International Journal of Multiphase Flow 55 (2013) 64–79

Contents lists available at SciVerse ScienceDirect

International Journal of Multiphase Flow

journal homepage: www.elsevier.com/locate/ijmulflow

Eulerian–Lagrangian modeling of turbulent liquid–solid slurries in horizontal pipes

Jesse Capecelatro *, Olivier Desjardins

Sibley School of Mechanical and Aerospace Engineering, Cornell University, Ithaca, NY 14853, USA

ARTICLE INFO

Article history:
Received 29 March 2013
Received in revised form 22 April 2013
Accepted 27 April 2013
Available online 9 May 2013

Keywords:
Eulerian Lagrangian
Liquid–solid
Sediment transport
Particle tracking
Slurry
Pipelines
Deposition

ABSTRACT

Computations of liquid–solid slurries in horizontal pipes are performed to investigate the complex multiphase flow dynamics associated with operating conditions above and below the critical deposition velocity. A high-fidelity large eddy simulation framework is combined with a Lagrangian particle tracking solver to account for polydispersed settling particles in a fully developed turbulent flow. The two phases are fully coupled via volume fraction and momentum exchange terms, and a two-step filtering process is employed to alleviate any dependence of the liquid-phase mesh size on the particle diameter, enabling the capture of a wide range of spatial turbulent scales. A fully conservative immersed boundary method is employed to account for the pipe geometry on a uniform Cartesian mesh. Two cases are simulated, each with a pipe geometry and particle size distribution matching an experimental study from Roco & Balakrishnam, which considers a mean volumetric solid concentration of 8.4%, corresponding to just over 16 million particles. The first case considers a Reynolds number based on the bulk flow of the liquid of 85,000, resulting in a heterogeneous suspension of particles throughout the pipe cross-section. Statistics on the concentration and velocity of the particle phase for this case show excellent agreement with experimental results. The second case considers a lower Reynolds number of 42,660, leading to the formation of a stationary bed of particles. Three distinct regions are identified in the second case, corresponding to a rigid bed at the bottom of the pipe, a highly-collisional shear flow just above the bed, and a dilute suspension of particles far from the bed. Computational results indicate segregation in particle size along the vertical direction, with the smallest particles located at the top, increasing monotonically until the bed surface, where the largest particles are located. The covariance of concentration and velocity of each phase is presented, giving further insight on the multiphase dynamics. Statistics on the individual mechanisms that contribute to the motion of each particle, namely forces due to drag, the pressure gradient and viscous stresses of the surrounding fluid, and collisions, are provided for each case. It is observed that for the majority of the pipe cross-section, the drag force dominates for each case, which is balanced by inter-particle collisions in the streamwise direction, and by gravity in the vertical direction. Simulation results are also used to investigate closures from Reynolds average modeling of multiphase flows.

1. Introduction

Liquid–solid two phase flows, referred to as slurries, are common in many engineering and natural processes, and are often turbulent. Due to the relatively low operation and maintenance costs, slurry pipelines are typically used in chemical and mining industries for long distance transport of bulk materials such as oil sand ore, coal, copper, iron and phosphate concentrates, among others, to processing plants. The slurry consists of settling particles in a turbulent carrier fluid, where the solid material is usually polydisperse with a size distribution that can span several orders of magnitude. At very high flow rates the solid particles are nearly uniformly distributed across the pipe cross-section due to the high level of turbulence. Reduction in the flow rate leads to a higher concentration of particles at the bottom of the pipe. As the velocity continues to decrease, the solid material may form a dense sliding bed and eventually a stationary bed. The bulk slurry velocity associated with the onset of a stationary bed is referred to as the critical deposition velocity. The formation of a bed layer can be very hazardous, leading to wear and possible blockage of the pipeline. The frictional pressure loss is a key parameter in the design of slurry pipelines, as it provides information on the power required to maintain a flow rate above the critical deposition velocity. The solid velocity profile, slip velocity between the phases, solid concentration profile, and particle size distribution all impact the

* Corresponding author. Tel.: +1 8456612336.
E-mail address: jsc359@cornell.edu (J. Capecelatro).

0301-9322/$ - see front matter © 2013 Elsevier Ltd. All rights reserved.
http://dx.doi.org/10.1016/j.ijmultiphaseflow.2013.04.006

pressure drop in the pipe. However, the wide range of length and time scales associated with dispersed multiphase flows makes estimations of these parameters extremely difficult.

Great effort has been made towards the development of predictive and reliable models for the pressure drop and solids concentration distribution in slurry pipelines. Durand and Condolios (1952) were some of the first to develop empirical models for computing the hydraulic gradient, suggesting that the Froude number, specific gravity, concentration of particles, and particle drag coefficient are key parameters. Wasp et al. (1977) improved their calculation by incorporating the effect of varying-size particles with the assumption that a wide particle size distribution leads to better suspension. Kaushal and Tomita (2002) modified the Wasp et al. (1977) model by alleviating some of its restrictive assumptions, showing good agreement with laboratory experiments. Wilson (1976) used a force balance concept to develop a two-layer model where each layer has a uniform concentration and phase-averaged velocity, which was later improved by a three-layer model proposed by Doron et al. (1987) by including a stationary bed at low flow rates. Among these, the Saskatchewan Research Council (SRC) two-layer model of Gillies et al. (1991) is most commonly used in the literature for predicting the pressure drop in slurry pipelines. The SRC two-layer model predicts the pressure gradient and deposition velocity as a function of the particle diameter, pipe diameter, particle concentration, and the mixture velocity based on experimental correlations.

The extensive variety of modeling approaches that exist tends to lead to significantly varying predictions of the critical parameters. Furthermore, the vast majority of these models predict slurry flows without deposition taking place, and are only valid well above the critical deposition velocity. However, it is not always practical to avoid the formation of a bed at the bottom of the pipe, and very limited data is available in the literature for flows in this regime, even though this regime is of great practical importance. Several experiments have shown that the critical deposition velocity remains fairly constant for a wide range of solid loading. Kaushal and Tomita (2002) observed that the deposition velocity increases only by a very little amount as solid concentration increases. Schaan et al. (2000) saw a similar trend in the flow of various granular material through a 105 mm diameter pipe, reporting that overall the deposition velocity is fairly constant over the range of solid concentrations from 5% to 45% by volume. Further modeling challenges include the lack of data on particle segregation of polydisperse slurries. Kumar et al. (2003) show that the pressure drop and deposition velocity is greatly affected by the particle size distribution, though most of the experimental studies used to develop models for pressure drop considered monodisperse or narrow-size distributions. In addition, these models tend to provide information on macroscale features only, while local dynamics can affect pipeline operation significantly. Advancements in the understanding and prediction of detailed processes that contribute to pipeline wear, particle attrition, and agglomeration, is crucial.

With increasing computational resources and advancements in numerical modeling, computational fluid dynamics (CFD) is becoming a valuable tool for investigating slurry flows. CFD has the capability to generate detailed information of three-dimensional particle-laden flows under a wide range of operating conditions. However, directly solving the flow around each particle remains overly expensive for engineering systems of interest, which has led to the development of a large number of modeling approaches (see e.g. Capecelatro and Desjardins, 2012; Fox, 2012; Balachandar and Eaton, 2010; Deen et al., 2007; Patankar and Joseph, 2001; Van der Hoef et al., 2006). In recent years, liquid–solid slurries have been mostly simulated using Eulerian-based models for the solid phase and Reynolds Averaged Navier–Stokes (RANS) approaches to model the turbulent nature of the carrier fluid. Ling et al. (2003) proposed a simplified 3D algebraic slip mixture (ASM) model for the numerical computation of sand-water slurry flows. ASM was coupled with the renormalization group (RNG) K–ε turbulence model (Orszag et al., 1993) to obtain a solution in fully developed turbulent flows. They concluded that the model was capable of providing good predictions of the mean pressure gradient if the slurry mean velocity is higher than the critical deposition velocity, otherwise a big discrepancy existed between the numerical results and experimental data. Ekambara et al. (2009) obtained CFD results of horizontal liquid–solid slurry pipelines using ANSYS-CFX based on the kinetic theory of granular flow. They conducted several simulations with a range of flow parameters and compared local and time-averaged particle concentration profiles, particle and liquid velocity profiles, and frictional pressure loss with experimental data, showing overall good agreement. Concentration profiles compared best with fine-particulate slurries, but simulations were unable to reproduce experimental data when near-wall lift forces took effect. Kaushal et al. (2012) simulated pipeline slurry flows of monodisperse fine particles using a Eulerian two-phase model. Simulations were conducted for a range of concentrations and mixture velocities and gave fairly accurate predictions for both the pressure drop and concentration profiles. They presented velocity and slip-velocity distributions that had otherwise not been measured experimentally at such high particle concentrations. Overall, Eulerian-based methods are capable of producing accurate velocity and particle concentration profiles provided they have been appropriately tuned, and they have the advantage of representing a large number of particles at relatively low computational cost. However, detailed microscale and mesoscale information of the flow is compromised, and an accurate description of the interactions between the interstitial fluid and solid phase is limited. In addition, higher order statistics of the critical flow parameters are out of reach in the context of RANS. In order to gain further insight on local processes and important mesoscale features of the flow, more detailed simulation approaches are required.

In this work, individual particle trajectories are solved in a Lagrangian fashion, while the fully-developed turbulent flow is solved on a background Eulerian mesh in a large eddy simulation (LES) framework. The two phases are fully coupled via volume fraction and momentum exchange terms. A two-step filtering process is employed during interphase exchange, allowing for Eulerian grid spacing to particle diameter ratios close to unity, enabling the capture of important flow features at the particle scale. This simulation strategy has proven to be very successful for simulating dense gas–solid particulate flows (Capecelatro and Desjardins, 2012), and is employed for liquid–solid flows in this work. The equations of motion for each phase are presented in Section 2, followed by some details on the numerical implementation and simulation cases. In Section 3, simulations of three-dimensional polydisperse slurries in a horizontal pipe are presented. Two cases are considered, one operated above the critical deposition velocity, leading to a heterogeneous suspension of particles, and another below the critical deposition velocity, leading to a stationary bed. Results for the first case are compared with laboratory data from Roco and Balakrishnam (1985). A detailed investigation of both cases is then presented, providing mean and cross-correlation statistics of particle concentration, velocity, and slip velocity. Lagrangian statistics, including particle segregation and individual forces acting on each particle, are analyzed and discussed. Finally, in Section 4 the simulation results are used to study closures from RANS modeling of turbulent multiphase flows.

2. Governing equations and numerical implementation

This section summarizes the equations used to describe the motion of particle trajectories suspended in a wall-bounded liquid

flow, and presents the numerical framework and simulation parameters considered in this study.

2.1. Fluid equations

To solve the equations of motion for the liquid in the slurry without requiring to resolve the flow around individual particles, a volume filtering operator is applied to the Navier–Stokes equations, thereby replacing the point variables (fluid velocity, pressure, etc.) by smoother, locally filtered fields. Following the work of Anderson and Jackson (1967), which was then extended by Capecelatro and Desjardins (2012), the volume-filtered continuity equation is given by

$$\frac{\partial}{\partial t}(\varepsilon_f \rho_f) + \nabla \cdot (\varepsilon_f \rho_f \boldsymbol{u}_f) = 0, \tag{1}$$

where ε_f, ρ_f, and $\boldsymbol{u}_f$ are the fluid-phase volume fraction, density, and velocity, respectively. The momentum equation is given by

$$\frac{\partial}{\partial t}(\varepsilon_f \rho_f \boldsymbol{u}_f) + \nabla \cdot (\varepsilon_f \rho_f \boldsymbol{u}_f \otimes \boldsymbol{u}_f) = \nabla \cdot (\boldsymbol{\tau} - \boldsymbol{R}_u) + \varepsilon_f \rho_f \boldsymbol{g} - \boldsymbol{F}^{\text{inter}} + \boldsymbol{F}^{\text{mfr}}, \tag{2}$$

where $\boldsymbol{g}$ is the acceleration due to gravity, and $\boldsymbol{F}^{\text{inter}}$ is the interphase exchange term that arises from filtering the divergence of the stress tensor, which will be described in detail in Section 2.2. $\boldsymbol{F}^{\text{mfr}}$ is a body force akin to a mean pressure gradient introduced to maintain a constant mass flow rate in the pipe, and will be defined later in Section 2.3. The volume-filtered stress tensor, $\boldsymbol{\tau}$, is expressed as

$$\boldsymbol{\tau} = -p\mathcal{I} + \mu\left[\nabla \boldsymbol{u}_f + \nabla \boldsymbol{u}_f^{\top} - \frac{2}{3}(\nabla \cdot \boldsymbol{u}_f)\mathcal{I}\right] + \boldsymbol{R}_\mu, \tag{3}$$

where the hydrodynamic pressure and dynamic viscosity are given by p and μ, respectively. $\mathcal{I}$ is the identity tensor. $\boldsymbol{R}_\mu$ is an unclosed term that arises as a result of filtering the velocity gradients in the point wise stress tensor, and is modeled by introducing an effective viscosity μ^* to account for enhanced dissipation by the particles, given by

$$\boldsymbol{R}_\mu \approx \mu^*\left[\nabla \boldsymbol{u}_f + \nabla \boldsymbol{u}_f^{\top} - \frac{2}{3}(\nabla \cdot \boldsymbol{u}_f)\mathcal{I}\right], \tag{4}$$

where μ^* was derived by Gibilaro et al. (2007) for fluidized beds, and is given by

$$\mu^* = \mu\left(\varepsilon_f^{-2.8} - 1\right). \tag{5}$$

In Eq. (2), $\boldsymbol{R}_u$ is a sub-filter Reynolds stress term closed through a turbulent viscosity model, given by

$$\boldsymbol{R}_u \approx \mu_t\left[\nabla \boldsymbol{u}_f + \nabla \boldsymbol{u}_f^{\top} - \frac{2}{3}(\nabla \cdot \boldsymbol{u}_f)\mathcal{I}\right]. \tag{6}$$

A dynamic Smagorinsky model (Germano et al., 1991; Lilly, 1992) based on Lagrangian averaging (Meneveau et al., 1996) is employed to estimate the turbulent viscosity μ_t.

2.2. Lagrangian particle tracking

The displacement of an individual particle indicated by the subscript p is calculated using Newton's second law of motion,

$$m_p \frac{d\boldsymbol{u}_p}{dt} = \boldsymbol{f}_p^{\text{inter}} + \boldsymbol{F}_p^{\text{col}} + m_p \boldsymbol{g}, \tag{7}$$

where the particle mass is defined by $m_p = \pi \rho_p d_p^3/6$, where ρ_p and d_p are the particle density and diameter, respectively. The force $\boldsymbol{f}_p^{\text{inter}}$ exerted on a single particle p by the surrounding fluid is related to the interphase exchange term in Eq. (2) by

$$\boldsymbol{F}^{\text{inter}} = \sum_{p=1}^{n_p} \xi(|\boldsymbol{x} - \boldsymbol{x}_p|)\boldsymbol{f}_p^{\text{inter}}, \tag{8}$$

where n_p is the total number of particles, ξ is the filtering kernel, $\boldsymbol{x}_p$ is the position of the pth particle, and $\boldsymbol{f}_p^{\text{inter}}$ is approximated by

$$\boldsymbol{f}_p^{\text{inter}} \approx \mathcal{V}_p \nabla \cdot \boldsymbol{\tau} + \boldsymbol{f}_p^{\text{drag}}, \tag{9}$$

where $\mathcal{V}_p$ is the volume of the pth particle. The drag force is given as

$$\frac{\boldsymbol{f}_p^{\text{drag}}}{m_p} = \frac{1}{\tau_p}(\boldsymbol{u}_f - \boldsymbol{u}_p)F(\varepsilon_f, \text{Re}_p), \tag{10}$$

where the particle response time τ_p derived from Stokes flow is

$$\tau_p = \frac{\rho_p d_p^2}{18\mu\varepsilon_f}. \tag{11}$$

The dimensionless drag force coefficient of Tenneti et al. (2011) is employed in this work, which is valid for a wide range of Reynolds numbers and solid packing, given by

$$F(\varepsilon_f, \text{Re}_p) = \frac{1 + 0.15\text{Re}_p^{0.687}}{\varepsilon_f^2} + \varepsilon_f F_1(\varepsilon_f) + \varepsilon_f F_2(\varepsilon_f, \text{Re}_p), \tag{12}$$

where the particle Reynolds number is

$$\text{Re}_p = \frac{\varepsilon_f \rho_f |\boldsymbol{u}_f - \boldsymbol{u}_p| d_p}{\mu}. \tag{13}$$

The remaining two terms are given by

$$F_1(\varepsilon_f) = \frac{5.81\varepsilon_p}{\varepsilon_f^3} + \frac{0.48\varepsilon_p^{1/3}}{\varepsilon_f^4},$$

$$F_2(\varepsilon_f, \text{Re}_p) = \varepsilon_p^3 \text{Re}_p\left(0.95 + \frac{0.61\varepsilon_p^3}{\varepsilon_f^2}\right),$$

where $\varepsilon_p = 1 - \varepsilon_f$ is the particle-phase volume fraction. More details are provided in Capecelatro and Desjardins (2012).

Other contributions to the interphase exchange include the added mass term, Basset history term, lift, and Faxen forces. Zhang and Prosperetti (1994) give an exact expression for the added mass term for an inviscid fluid at low particle concentrations. At higher values of concentration, they include a correction to account for the local volume fraction. They also derive an expression for the lift force for spherical particles in an inviscid fluid. A quite different expression is given by Saffman (1965) for viscous flows at low Reynolds numbers. Kaushal and Tomita (2007) studied the effect of near-wall lift forces in slurries using a γ-ray densitometer. They observed a decrease in lift with increased flow rate, and concluded that there is an absence of near-wall lift for finer particles while the near-wall lift related to coarser particles is not associated with the Magnus effect, the Saffman force, or other lift-like interaction forces. Although lift effects may have non-negligible contributions to the mean motion of the particles, a broad agreement on an appropriate model for this expression does not exist. Models for the lift coefficient found in the literature are typically valid for a single isolated particle, and become inaccurate for deposition near solid boundaries and high particle Reynolds numbers (Wang et al., 1997; Kurose and Komori, 1999). As a consequence, such contributions are not considered in this work. However, since we account for the volume filtered fluid pressure gradient force and viscous stress at the location of each particle explicitly, some of these effects are captured.

The angular momentum of the particle, ω_p, is attributed to particle collisions only, and is given by

$$I_p \frac{d\boldsymbol{\omega}_p}{dt} = \sum_j \frac{d_p}{2}\boldsymbol{n} \times \boldsymbol{f}_{t,j\to p}^{\text{col}}, \tag{14}$$

where $\boldsymbol{f}^{\text{col}}_{t,j\to p}$ is the tangential component of the collision force of particle j acting on particle p, and I_p is the moment of inertia of the particle, given for a sphere by

$$I_p = \frac{m_p d_p^2}{10}. \tag{15}$$

Particle–particle and particle–wall collisions are modeled using a soft-sphere approach originally proposed by Cundall and Strack (1979). When two particles come into contact, a repulsive force $\boldsymbol{f}^{\text{col}}_n$ is created as

$$\boldsymbol{f}^{\text{col}}_{n,b\to a} = \begin{cases} -k\delta_{ab}\boldsymbol{n}_{ab} - \eta \boldsymbol{u}_{ab,n} & \text{if } d_{ab} < (r_a + r_b + \lambda), \\ 0 \quad \text{else}, \end{cases} \tag{16}$$

where r_a and r_b are the radii of particles a and b, respectively, d_{ab} is the distance between the centers of the particles, δ_{ab} is the overlap between the particles, and $\boldsymbol{n}_{ab}$ is the unit normal vector from particle a to particle b. A sketch of the collision process is given in Fig. 1. The normal relative velocity between particles a and b is given by

$$\boldsymbol{u}_{ab,n} = ((\boldsymbol{u}_a - \boldsymbol{u}_b)\cdot \boldsymbol{n}_{ab})\boldsymbol{n}_{ab}. \tag{17}$$

The spring stiffness and damping parameter are given by k and η, respectively. A model for the damping parameter uses a coefficient of restitution $0 < e < 1$ and an effective mass $m_{ab} = (1/m_a + 1/m_b)^{-1}$ such that

$$\eta = -2\ln e \frac{\sqrt{m_{ab}k}}{\pi^2 + (\ln e)^2}. \tag{18}$$

The spring stiffness is related to the collision time, τ_{col}, according to

$$k = m_{ab}/\tau_{col}^2(\pi^2 + (\ln e)^2). \tag{19}$$

To properly resolve the collisions without requiring an excessively small timestep, $\tau_{col} = 15\Delta t$ is chosen for all simulations presented in this work. λ is the force range, a small number that allows for collisions to initiate before particles are in contact, which decreases monotonically with decreasing particle velocity (Capecelatro and Desjardins, 2012). Collisions with walls are handled by treating the walls as particles with infinite mass and zero radius. To account for friction between particles and thus particle rotation, the static friction model is employed for the tangential component of the collision force, given by

$$\boldsymbol{f}^{\text{col}}_{t,b\to a} = -\mu_f |\boldsymbol{f}^{\text{col}}_{n,b\to a}| \boldsymbol{t}_{ab}. \tag{20}$$

The relative tangential velocity, $\boldsymbol{u}_{ab,t}$, is defined as

$$\boldsymbol{u}_{ab,t} = \boldsymbol{u}_{ab} - \boldsymbol{u}_{ab,n}, \tag{21}$$

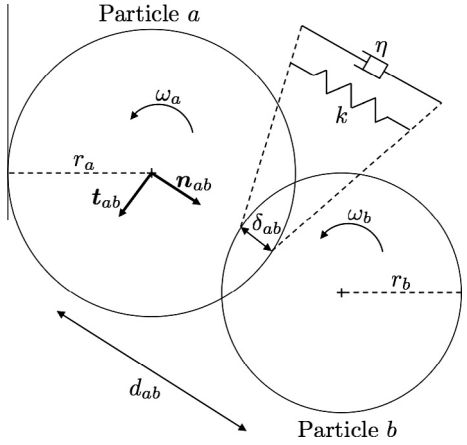

Fig. 1. Soft-sphere representation of two particles undergoing collision.

and is used to create a tangential unit vector $\boldsymbol{t}_{ab}$ as

$$\boldsymbol{t}_{ab} = \frac{\boldsymbol{u}_{ab,t}}{|\boldsymbol{u}_{ab,t}|}. \tag{22}$$

2.3. Momentum forcing

To simulate a fully-developed turbulent flow, periodic boundary conditions are used in the streamwise direction. In order to maintain a constant mass flow rate in this periodic environment, momentum is forced using a uniform source term that is adjusted dynamically in Eq. (2). This source term exactly reflects the mean pressure gradient required to maintain the flow rate. At each timestep, momentum is lost via drag on the particles and viscous fluxes at the walls, which must be added back to the momentum equation. Volume integrating Eq. (2) and rearranging leads to

$$\boldsymbol{F}^{\text{mfr}} = -\frac{1}{\mathcal{V}_f}\int_{\mathcal{V}_f} [\nabla\cdot(\boldsymbol{\tau} - \boldsymbol{R}_u) + \varepsilon_f \rho_f \boldsymbol{g} - \boldsymbol{F}^{\text{inter}}] d\mathcal{V}_f, \tag{23}$$

where $\mathcal{V}_f$ is the volume occupied by the fluid. Note that the pressure gradient term vanishes due to the periodic boundary condition. The source term is applied to Eq. (2), and is added to the pressure gradient in the filtered stress tensor in Eq. (9).

2.4. Numerical framework

To study the detailed mesoscale physics of slurries in horizontal pipes, the mathematical description presented heretofore is implemented in the framework of NGA (Desjardins et al., 2008), a high-order, fully conservative CFD code tailored for turbulent flow computations. The Navier–Stokes equations are solved on a staggered grid with second order spatial accuracy for both the convective and viscous terms, and the second order accurate semi-implicit Crank-Nicolson scheme of Pierce (2001) is implemented for time advancement. The details on the mass, momentum, and energy conserving finite difference scheme are available in Desjardins et al. (2008).

The particles are distributed among the processors based on the underlying domain decomposition of the liquid phase. For each particle, its position, velocity, and angular velocity are solved using a second-order Runge–Kutta scheme. Sub-stepping is used to ensure stability when the particle response time (defined in Eq. (11)) becomes smaller than the simulation timestep. Coupling between the liquid phase and solid particles appears in the form of the volume fraction ε_f, and interphase exchange term $\boldsymbol{F}^{\text{inter}}$ defined by Eq. (8). These terms are first computed at the location of each particle, using information from the fluid, and are then transferred to the Eulerian mesh. To interpolate the fluid variables to the particle location, a second order trilinear interpolation scheme is used. To extrapolate the particle data back to the Eulerian mesh in a computationally efficient manner that is consistent with the mathematical formulation, a two-step mollification/diffusion operation is employed. This strategy has been shown to be both conservative and converge under mesh refinement (Capecelatro and Desjardins, 2012). A proper parallel implementation makes simulations consisting of $\mathcal{O}(10^8)$ Lagrangian particles possible, allowing for a detailed numerical investigation of slurries with realistic physical parameters and moderate concentrations.

The liquid-phase transport equations are discretized on a Cartesian mesh, and a conservative immersed boundary (IB) method is employed to model the cylindrical pipe geometry without requiring a body-fitted mesh. The method is based on a cut-cell formulation that requires rescaling of the convective and viscous fluxes in these cells, and provides discrete conservation of mass and momentum (Meyer et al., 2010; Pepiot and Desjardins, 2010).

Details on coupling the IB method with the Lagrangian particle solver can be found in Capecelatro and Desjardins (2012).

2.5. Configuration and simulation parameters

The simulations conducted in this work are modeled after the experiments presented by Roco and Balakrishnam (1985). A 5.15 cm diameter pipe with a mean particle volume fraction of 8.4% is considered, illustrated in Fig. 2a. The slurry consists of sand with a mean diameter of 165 μm ranging from 50 to 307 μm, suspended in water. The particle size distribution in the simulation resembles that of the experiment, shown in the cumulative distribution function (CDF) in Fig. 2b. Periodic boundary conditions are enforced in the x-direction. The pipe length was chosen to be as long as possible while remaining computationally tractable. With this consideration, an aspect ratio of 5 was chosen, corresponding to over 16 million particles and 18.7 million grid cells. A cell size approximately equal to the maximum particle diameter was chosen in order to best capture the range of spatial scales associated with the turbulent flow. The complete set of simulation parameters is given in Table 1.

Two cases are considered by keeping all parameters constant and varying only the liquid bulk velocity U_f. Case A has a bulk velocity of 1.6 m/s, resulting in a heterogeneous suspension of particles with a liquid Reynolds number $\mathrm{Re} = \rho_f U_f D/\mu = 85{,}000$. A slurry with a stationary bed is considered in case B, where the Reynolds number is decreased to 46,660, corresponding to $U_f = 0.83$ m/s, well below the critical deposition velocity of 1.2 m/s predicted by the model of Wasp et al. (1977).

3. Results

3.1. Flow characterization

In both simulations, the flow organizes into distinct regions controlled by the dynamics of the flow. To help guide the analysis and discussion of the computational results, these distinct layers are depicted by the thin gray lines in the subsequent figures. Three flow regions are easily identified in case B, denoted throughout as region I, II, and III. Region I corresponds to the rigid bed located at the bottom of the pipe, up to $y/D = -0.405$. The particles in the bed are densely packed and undergo sustained contact, and as a result do not contribute to the mean motion of the flow. Located just above the bed, region II extends up to ε_p approximately equal to 0.25, which corresponds to $y/D = -0.328$, and consists of highly collisional particles and high liquid turbulence intensity. In this region, particles can be lifted from the bed by strong turbulent eddies or ejected by other particles colliding with the bed. Finally, region III is located far from the bed such that the mean particle concentration is considerably smaller and the particles remain suspended due to liquid velocity fluctuations.

The distinction between the flow regions in case A is less obvious. In this case, there is no formation of a bed at the bottom of the pipe, and instead the flow is divided into regions II and III only. The transition between these regions was chosen to correspond to a concentration similar to the transition between regions II and III in case B. To avoid overly confusing figures, the transition between regions II and III corresponds to the location of the interface separating regions I and II in case B at $y/D = -0.405$.

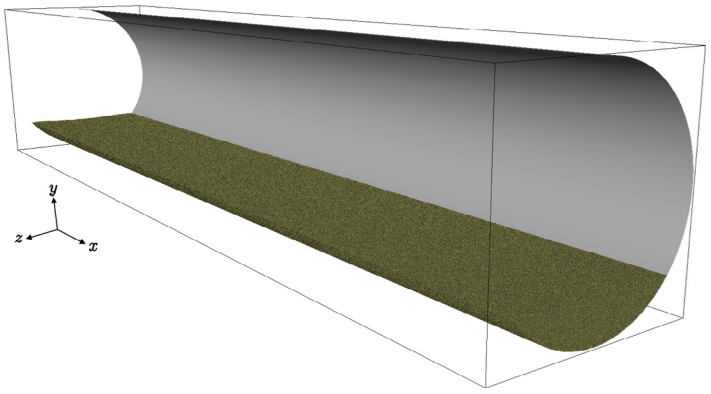

(a) Initial particle distribution and pipe geometry. 8.4% concentration of particles by volume, corresponding to 16 million particles.

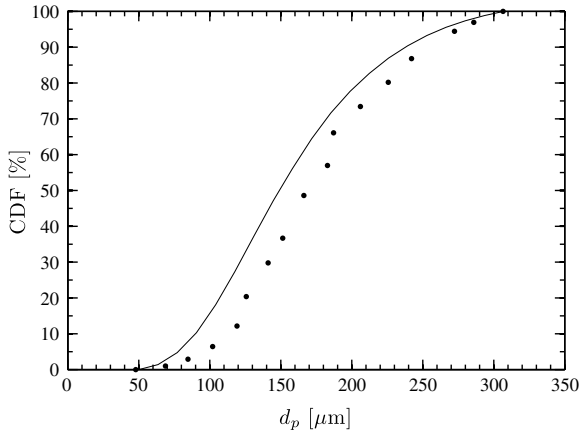

(b) CDF of particle diameter. Experimental data (circles), simulation data (line).

Fig. 2. Simulation geometry and particle size distribution.

Table 1
Simulation parameters for each case. $St = \tau_p u_\tau^2 \rho_f / \mu$, where the frictional liquid velocity u_τ is computed using Prandtl's friction law for smooth pipes (Pope, 2000).

Pipe diameter, D	5.15	cm		
Pipe length	25.75	cm		
Cells in x-direction, nx	768	–		
Cells in y-direction, ny	156	–		
Cells in z-direction, nz	156	–		
Number of particles, n_p	16,027,332	–		
Mean particle concentration	0.084	–		
Mean particle diameter	165	μm		
Minimum particle diameter	50	μm		
Maximum particle diameter	307	μm		
Particle standard deviation	70	μm		
Particle density, ρ_p	2650	kg/m^3		
Particle–particle coefficient of restitution	0.9	–		
Particle–wall coefficient of restitution	0.8	–		
Coefficient of friction	0.1	–		
Case	A		B	
Bulk liquid velocity, U_f	1.6	m/s	0.83	m/s
Stokes number, St	23.8	–	7.4	–
Timestep, Δt	4×10^{-6}	s	2×10^{-5}	s

3.2. Comparison with experiments

Experimental results of the local, time-averaged particle concentration, particle velocity distribution, and frictional pressure drop are available for case A only. For each case, simulations were run long enough to reach a statistically stationary state. Results were collected after approximately $\tau = 50$, where $\tau = tU_f/D$ is the non-dimensional time. The mean quantities of interest, denoted by the brackets, were obtained by averaging in the x-direction, in time over approximately 70 non-dimensional time units, and by symmetry about the $z = 0$ plane. Most results are presented as a function of vertical distance for $z = 0$, denoted throughout as the central vertical axis or vertical centerline, or as a function of z for $y = 0$, denoted as the horizontal centerline. Simulation and experimental results of the particle concentration and velocity profiles along the vertical axis of the pipe are presented in Fig. 3. The distributions are asymmetric, with larger concentrations and lower velocities observed in the bottom half of the central vertical axis due to particle settling. While excellent agreement with the experiment is obtained, a slight over-prediction of particle concentration is observed in region II at the bottom of the pipe. This discrepancy may be attributed to the near-wall modeling challenges discussed in Capecelatro and Desjardins (2012), or a result of neglecting lift forces in Eq. (9).

Figs. 4 and 5 show contours of particle concentration and velocity in the cross-section of the pipe, respectively. Again, excellent agreement is observed with the experiment. From Fig. 4, it seen that the concentration in the lower third of the central vertical axis is approximately 10 times the concentration at the top third. In Fig. 5, a steeper gradient in particle velocity is observed at the top of the pipe compared to the bottom.

Finally, the reported experimental pressure drop for this case is −666.3 Pa/m. The pressure drop determined using Eq. (23) was found to be −510 Pa/m. This discrepancy is attributed to errors in the calculation of the viscous flux at the IB surface and inaccuracies in the near-wall modeling in the context of LES.

3.3. Operating below the critical deposition velocity

Slurry pipelines operated below the critical deposition velocity can severely degrade performance and lead to blockage and equipment failure. At low flow rates, the liquid shear stress cannot overcome the submerged weight of the particles, allowing particles to settle and form a stationary bed. Case B was simulated with a bulk velocity of 0.83 m/s, well below the critical deposition velocity of 1.2 m/s predicted by the model of Wasp et al. (1977) for the parameters given in Table 1. Fig. 6a and b show the mean particle concentration and velocity profiles for that case along the central vertical axis of the pipe. Note that due to polydispersity, the random-close-packing limit for hard spheres, $\varepsilon_{p,\ \max} = 0.634$, is exceeded. The liquid velocity profiles for both cases are not shown due to the similarities with the particle phase, and instead the relative velocity between the two phases will be provided in Section 3.5. The solid concentration profile in Fig. 6a shows that the particles are almost entirely located in the bottom half of the pipe. The solid concentration is nearly constant in region I and decreases rapidly in region II. As seen in Fig. 6b, the particle velocity is very small in region I, and increases rapidly in region II. Above the bed, the solid velocity profile in case B resembles the profile of case A in Fig. 3b.

The degree of particle accumulation can be quantified by the probability density function (PDF) of particle number density (Pozorski and Apte, 2009), which is equivalent to the PDF of particle concentration. For a random distribution of particles, in the absence of any processes leading to segregation (e.g., particle settling due to gravitation effects or turbophoresis as a result of turbulence in the carrier phase), a discrete Poisson distribution is expected, defined as

$$f_p(n_c) = \frac{e^{-\langle n_c \rangle}}{n_c!} \langle n_c \rangle^{n_c}, \tag{24}$$

where n_c is the number of particles per computational cell and $\langle n_c \rangle$ is the average number of particles per computational cell. The Poisson distribution is computed by considering particles with a diameter of 165 μm, i.e. the mean diameter of the distribution used in the simulations. The PDF of particle concentration for each case along with the discrete Poisson distribution is given in Fig. 7. As can be expected from the large variation in particle concentration observed in Fig. 3a and Fig. 6a, both cases show a higher frequency of regions containing more particles, as well as regions devoid of particles, in comparison to the Poisson distribution. These traits are more pronounced for case B than for case A, and in fact for that case the distribution is bi-modal, reflecting the large number of particles around the close-packing limit that constitute the bed.

The joint-PDFs of Re_p and ε_p for both cases are displayed in Fig. 8. The joint-PDF was computed using the Reynolds number of each particle and the volume fraction interpolated to the position of the respective particle. Several differences can be observed between each case. Due to the presence of the bed, case B shows a very high frequency of low Re_p particles near the close packing limit, while a somewhat wider range of Re_p values is reached for

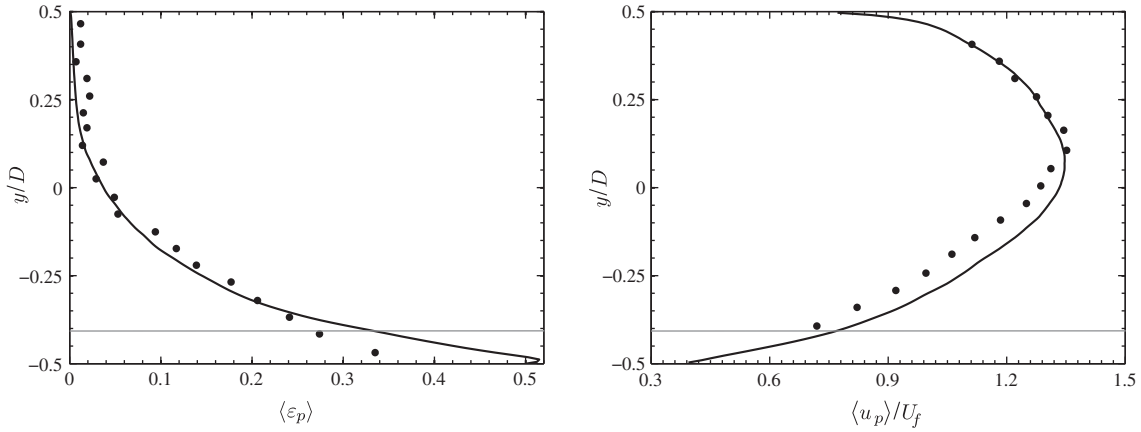

(a) Solid concentration profile.

(b) Solid velocity profile normalized by the bulk fluid velocity.

Fig. 3. Mean statistics along the central vertical axis of the pipe for case A. Experimental data (Roco and Balakrishnam, 1985) (circles), simulation results (thick solid line), boundary separating regions II and III (thin solid line).

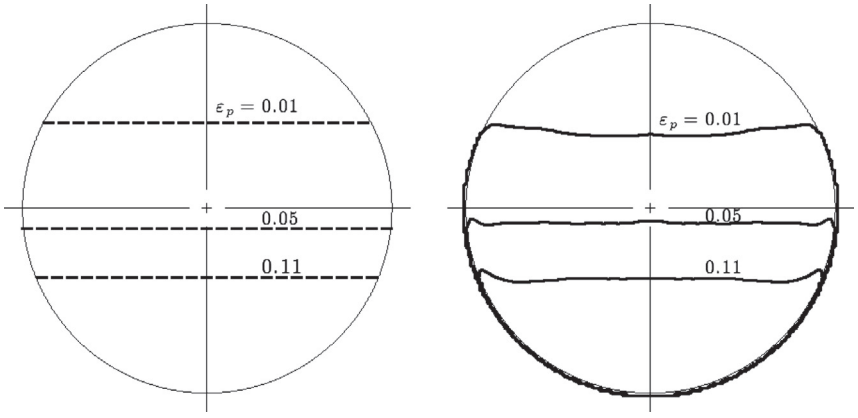

(a) Experimental data (Roco and Balakrishnam, 1985).

(b) Simulation results.

Fig. 4. Particle concentration distribution in the pipe cross-section for case A.

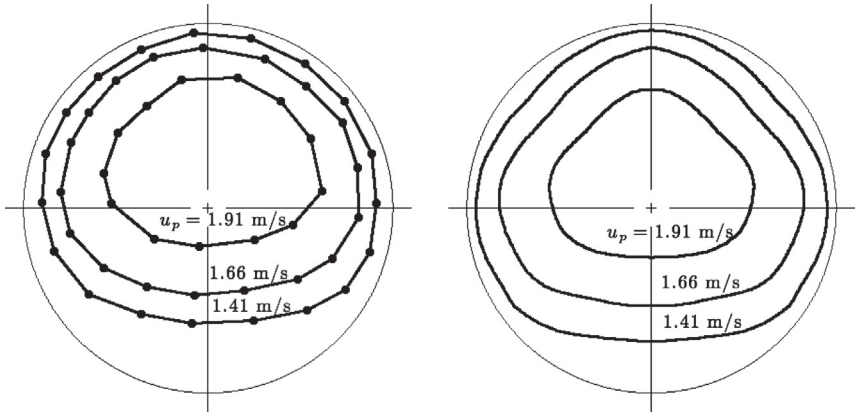

(a) Experimental data (Roco and Balakrishnam, 1985).

(b) Simulation results.

Fig. 5. Particle velocity distribution in the pipe cross-section for case A.

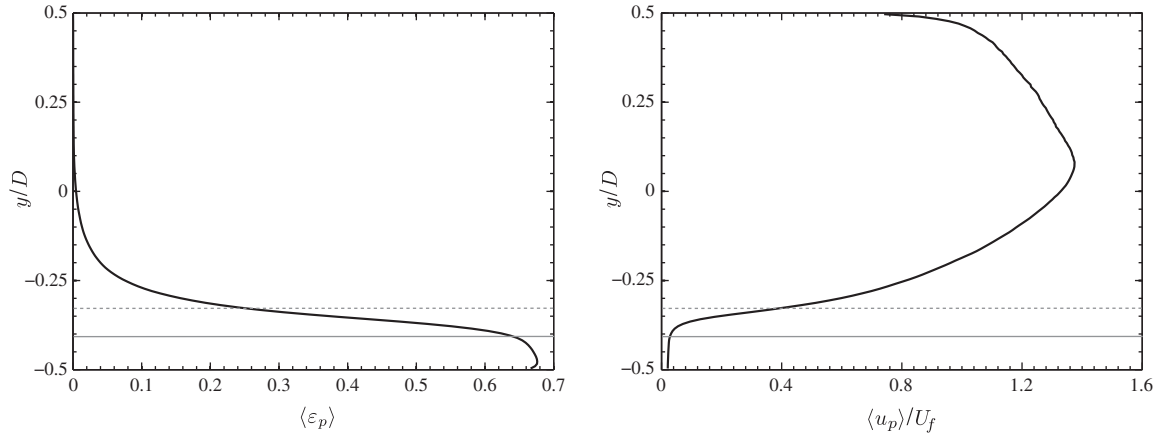

(a) Solid concentration profile. (b) Solid velocity profile.

Fig. 6. Mean statistics along the central vertical axis of the pipe for case B. Transition between regions I and II (gray solid line), transition between regions II and III (gray dotted line).

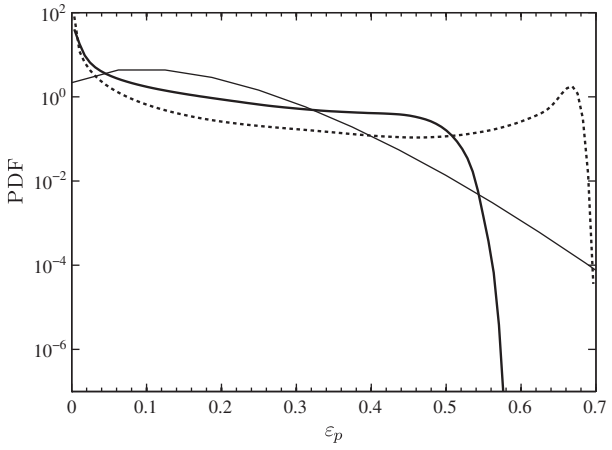

Fig. 7. PDF of particle concentration. Case A (thick solid line), case B (dashed line), Poisson distribution (thin solid line).

particles in low ε_p regions. In comparison, case A displays much larger values of Re_p that correspond to a wide range of ε_p.

3.4. Higher order statistics

Higher order statistics are extracted from both simulations in order to gain further insight on the multiphase dynamics. The particle concentration variance is displayed in Fig. 9. For case B, the greatest concentration fluctuations are located at the interface between region II and region III. In region III, the fluctuations decay rapidly to very small values due to the dilute nature of the flow in that layer. The bed region, region I, exhibits no variance in concentration, indicative of particles remaining in rigid contact. In comparison, concentration fluctuations in case A are non-negligible at the bottom of the pipe, confirming that a stationary bed has not formed. Similarly to case B, the volume fraction variance for case A peaks near the bottom of region III, albeit at a lower value than case B. These fluctuations in case A remain noticeable throughout the majority of the pipe.

The components of the Reynolds stress tensor for both phases are displayed in Fig. 10. It can be noted that the particles have nearly the same fluctuation intensity as the liquid phase. For both cases, the greatest velocity fluctuations are located near the interface between region II and III, and at the top of the pipe. At the pipe center, turbulence production is minimum since the mean velocity gradient and shear stress are smallest, leading to small velocity fluctuations. In both simulations, $\left\langle u_p' v_p' \right\rangle$ and $\left\langle u_f' v_f' \right\rangle$ are negative in the bottom half of the central vertical axis and positive in the upper half, while the other components of the Reynolds stress tensor are positive throughout. The signs of the Reynolds stresses correspond to classical single phase wall-bounded turbulent flows (Pope, 2000). Fig. 10c and d reveal distinct trends of the velocity covariance profiles within the three regions of case B. In region I, the velocity covariance is negligibly small. In region II, the covariance magnitudes increase due to the nature of the highly collisional shear flow. In region III, the mean shear in the fluid decreases, leading to a decrease in the velocity covariance until contributions in shear from the upper wall in the pipe become significant. The behavior of the velocity covariance profiles along the vertical axis of case A resembles the trends seen in case B above the rigid bed.

Profiles of the covariance between concentration and velocity of each phase along the vertical axis of the pipe are displayed in Fig. 11. Again, note the similarities between particle and liquid statistics. From Fig. 11c and d, distinct trends are observed in the three regions in case B. The fluctuation magnitudes are smallest in the bed, increase within region II, and decrease in region III. Due to the small concentration of particles in the upper half of the central vertical axis, $\left\langle \varepsilon_p' \boldsymbol{u}_p' \right\rangle$ and $\left\langle \varepsilon_p' \boldsymbol{u}_f' \right\rangle$ are negligible in this region compared to the fluctuations in the lower half, though $\left\langle \varepsilon_p' w_p' \right\rangle$ and $\left\langle \varepsilon_p' w_f' \right\rangle$ are uncorrelated throughout the entire vertical axis due to the symmetry of the flow. The positive correlation of particle concentration and vertical velocity in region II and the lower half of region III reveals the tendency for local regions of high concentration to move upward, suggesting that groups of particles are drawn up from the bed surface into the more dilute regions. Since they originate from the surface of the stationary bed, these groups tend to move slower than the surrounding mixture in the streamwise direction, leading to a negative $\left\langle \varepsilon_p' u_p' \right\rangle$. To be compatible with a positive $\left\langle \varepsilon_p' v_p' \right\rangle$, it is expected that particles fall back down to the bed surface in more dilute arrangements. This behavior may be attributed to the presence of Kelvin–Helmholtz-type instabilities in region II, due to the high shear in mixture velocity and steep gradient in concentration. Fig. 12 confirms that longitudinal waves are visible in the instantaneous particle concentration field.

3.5. Slip velocity

The slip velocity, $\boldsymbol{u}_s = \boldsymbol{u}_f - \boldsymbol{u}_p$, is a critical parameter for understanding the behavior of slurry flows. For example, drag and lift

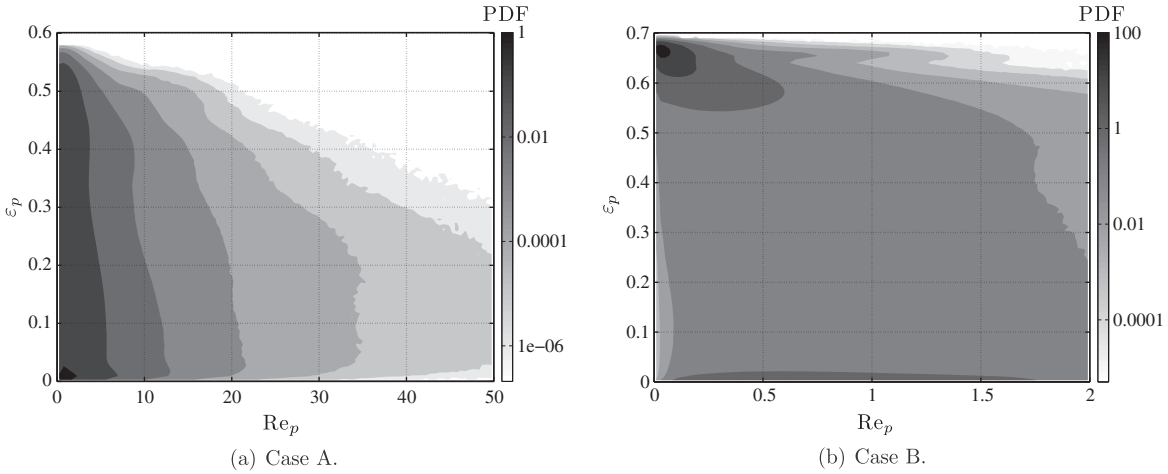

Fig. 8. Joint-PDF of particle Reynolds number and concentration.

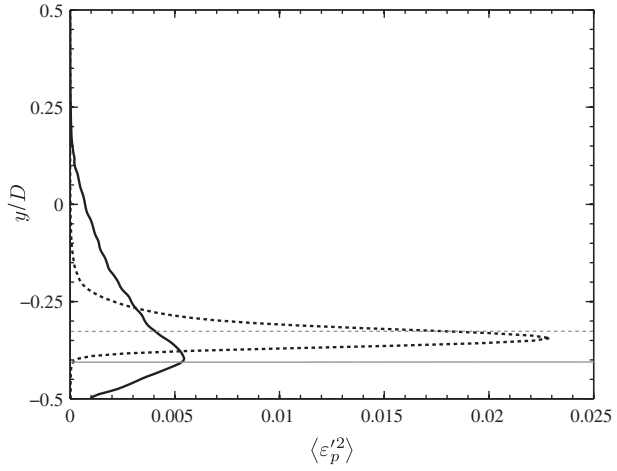

Fig. 9. Particle concentration variance profile along the central vertical axis of the pipe. Case A (thick solid line), case B (dashed line). The thin gray line separates regions II and III in case A and regions I and II in case B. The gray dotted line separates region II and III in case B.

forces strongly depend on $\boldsymbol{u}_s$, and knowledge of the relative velocities between phases can provide insight on deposition. Vertical and horizontal profiles of the mean and variance of the streamwise slip velocities along the pipe center are given in Fig. 13. Except for regions near the wall, the mean slip velocity magnitudes for both cases are relatively small, with maximum values approximately 0.05% of their respective bulk velocities. As seen in Fig. 13c, the mean slip velocity distribution is symmetric along the horizontal centerline, with negative values near the pipe wall. Particles located near the walls maintain their inertia while viscous effects reduce the liquid momentum, which explains these negative slip velocities. Symmetry is also observed in the slip velocity variance given in Fig. 13d, with maximum fluctuations near the pipe wall. However, it is evident from Fig. 13a and b that the slip velocity is asymmetric along the vertical centerline. It can be seen that except for the near-wall regions, the particle velocity lags behind the liquid velocity in both cases along the vertical axis. In case B, the slip velocity at the bottom of the pipe is negligible due to the presence of the bed. However, with the absence of a bed in case A, shear induced by the carrier phase leads to non-negligible particle contact forces in the streamwise direction, including normal collisions via Eq. (16) and Coloumb friction from Eq. (20), reducing the particle motion resulting in a zone of strong positive slip. Profiles of the forces exerted on the particles contributing to this behavior will be given in Section 3.6. This peak in slip velocity corresponds to the location of maximum solid concentration displayed in Fig. 3a. At the very bottom of the pipe, a negative slip velocity is recovered due to the fact that liquid does not slip while particles do. Fluctuations of the slip velocity along the vertical axis of the pipe are shown in Fig. 13b. In case A, $\langle u_s'^2 \rangle$ is fairly constant in the bottom portion of the pipe, and decreases at the pipe center. In case B, $\langle u_s'^2 \rangle$ is very small within the bed, increases in region II, and decreases in region III until near-wall effects at the top of the pipe become significant. From Fig. 10, the smallest slip velocity fluctuations correspond to the smallest velocity fluctuations.

3.6. Force balance

To gain further insight on the phenomenological behavior of both cases, the individual forces exerted on the particles are analyzed. In Fig. 14a and c, components of the streamwise particle acceleration are given along the vertical centerline. This includes the fluid drag given by Eq. (10), the volume-filtered pressure gradient, the volume-filtered viscous stress, and the collision force given by Eqs. (16) and (20). In case B, the competing interactions between these various forces can be distinguished between the three regions of the flow. In region I, drag is balanced by inter-particle collisions, leading to negligible streamwise acceleration. In region III, collisions are negligible and the fluid drag and pressure gradient forces dominate. A complex transition between both regions is observed in region II, with effects from inter-particle collisions, turbulence, and high shear velocities. These trends are not as clear in case A, which might be due in part to the transition from region II to III interacting with near-wall dynamics. In region II, the drag and collision forces dominate in the streamwise direction. In region III, the drag force dominates, although the pressure gradient and collision force remain significant.

The components of the vertical particle acceleration are displayed in Fig. 14b and d. At the bottom of the pipe, the drag force, pressure gradient, and collisions are balanced by gravity. In case B, the vertical drag force is negligible within the bed, and inter-particle collisions and the force due to the pressure gradient are approximately constant. In region II, the drag force increases rapidly and the collision force decreases until drag dominates in region III. Interestingly, the vertical force balance in regions I and II correspond the onset of fluidization observed in dense particle beds (Gidaspow, 1994). This behavior confirms that the vertical dynamics in region I correspond to a rigid bed, region III is drag

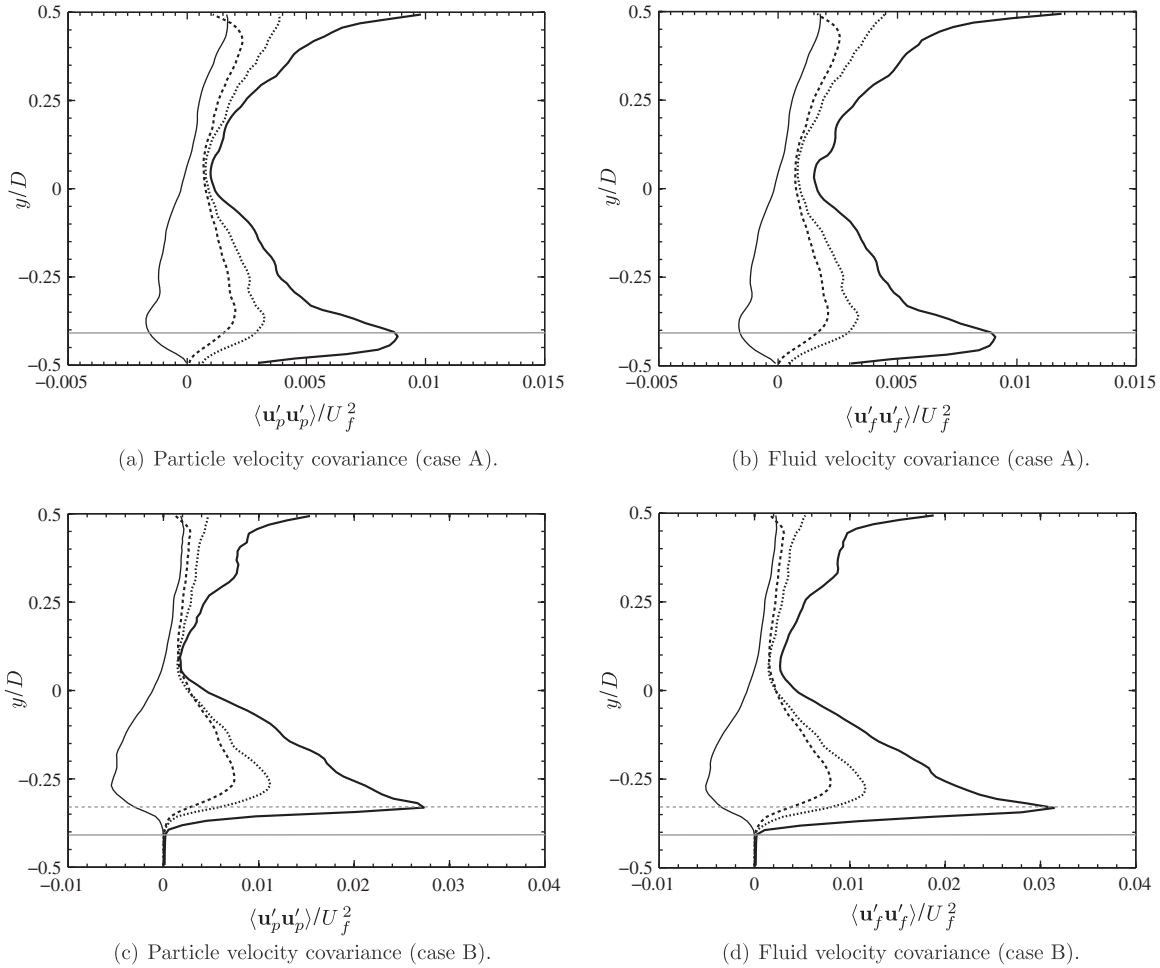

(a) Particle velocity covariance (case A).

(b) Fluid velocity covariance (case A).

(c) Particle velocity covariance (case B).

(d) Fluid velocity covariance (case B).

Fig. 10. Velocity covariance profiles normalized by the bulk fluid velocity along the central vertical axis of the pipe. $\langle u'u' \rangle$ (thick solid line), $\langle v'v' \rangle$ (dashed line), $\langle w'w' \rangle$ (dotted line), $\langle u'v' \rangle$ (thin solid line). The thin gray line separates regions II and III in case A and regions I and II in case B. The gray dotted line separates region II and III in case B.

dominated and the dynamics approach that of a dilute flow, and region II is a complex transition where all forces contribute to the mean motion of the particles. In case A, the vertical collision force is positive in region II and negative in the lower half of region III. The fluid pressure gradient and gravity have the greatest contributions to the motion of the particles in this region. In region III, the fluid pressure gradient decreases and drag rapidly dominates, as was observed for case B. In both cases, the force due to the filtered viscous stress has minimum effect on the motion of each particle.

3.7. Particle segregation

The particle size distribution can significantly impact the dynamics of liquid–solid slurries. For example, increasing the particle size will lead to an increase in the Coulomb friction force, resulting in an increase in pressure gradient and slip velocity. Larger particles will also lead to a larger gravitational force, which will enhance the settling rate and steepen the concentration gradient in the vertical direction. Kumar et al., 2003 measured the pressure drop and concentration distribution of particles for two materials mixed in different proportions to analyze this effect. It was found that in general, a slurry with a mixture of fine and coarse particles requires less energy for transportation. Interestingly, it was determined that the energy required to transport an optimally distributed mixture of particles is less than that required for a fine slurry. However, due to the strong coupling with the carrier phase turbulence and fluctuations in particle concentration, predictive modeling of particle segregation is particularly challenging.

Instantaneous snapshots of the particle position in a cross-sectional slice of the pipe are given in Fig. 15. A vertical gradient in particle diameter is observed in case A, with smaller particles at the top of the pipe and the largest at the bottom. In contrast, a layer of large particles is observed above the dense bed in case B. The mean particle diameter conditioned on the vertical height in the pipe is given in Fig. 16a, providing further detail on the particle segregation. Note that particle size averages are based on number density and not volume. The particle size is seen to decrease monotonically in the vertical direction in case A, except at the very bottom. Interestingly, in case B the slope reverses in region II where the particle size is shown to increase with height. It is postulated that particles are entrained by strong vortical structures directly above the surface of the bed, and the finest particles are ejected while the coarsest particles are too heavy and remain suspended in this region, unable to penetrate the dense bed in region I. To investigate the mechanisms responsible for this behavior, the distribution of vertical forces acting on each particle was computed for a range of particle sizes. The acceleration due to drag and the fluid pressure gradient is given in Fig. 17. Note that converging the results for the largest particles at the top of the pipe is challenging due to the small sample size, and are therefore not provided in all figures. As seen in Fig. 17b and d, the motion of each particle due to the fluid pressure gradient is not significantly affected by its diameter. However, from Fig. 17a and c, the vertical

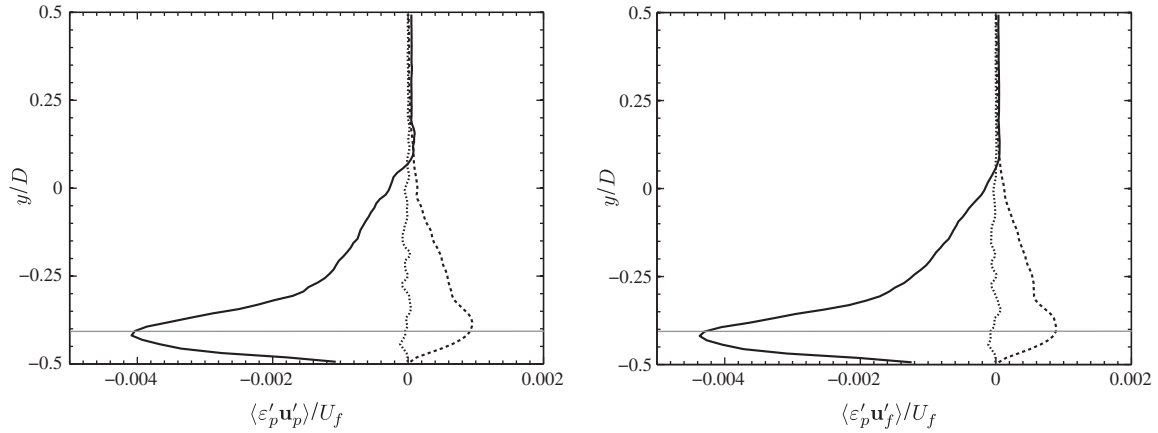

(a) Particle concentration-particle velocity covariance (case A).

(b) Particle concentration-fluid velocity covariance (case A).

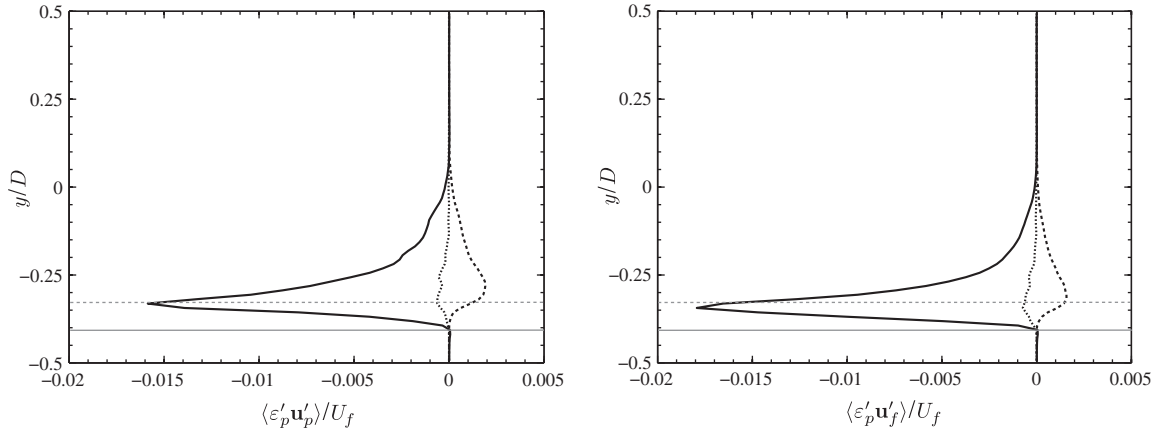

(c) Particle concentration-particle velocity covariance (case B).

(d) Particle concentration-fluid velocity covariance (case B).

Fig. 11. Particle concentration-velocity covariance profiles normalized by the bulk fluid velocity along the central vertical axis of the pipe. $\langle \varepsilon_p' u' \rangle$ (thick solid line), $\langle \varepsilon_p' v' \rangle$ (dashed line), $\langle \varepsilon_p' w' \rangle$ (dotted line). The thin gray line separates regions II and III in case A and regions I and II in case B. The gray dotted line separates region II and III in case B.

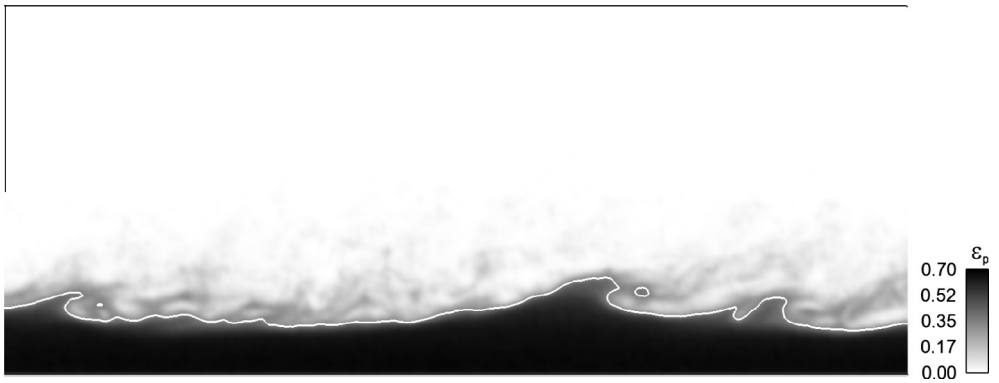

Fig. 12. Instantaneous snapshot of particle concentration in the $z = 0$ plane of case B. Iso-contour of $\varepsilon_p = 0.35$ given by the white line.

component of the acceleration due to drag is shown to be greatly affected by the particle size. In case B, the smallest particles experience the greatest vertical acceleration at the boundary between regions II and III. This behavior suggests that smaller particles are more likely to be ejected vertically than larger particles in this region.

Fluctuations in particle diameter are given in Fig. 16b. The greatest fluctuations are seen to correspond to the largest particles. In both simulations, the maximum fluctuation in particle size is located at the boundary between regions II and III, and the slope reverses below this boundary. In region I of case B, the particle diameter fluctuations are fairly constant. The PDF of particle diameter in each region of case B is given in Fig. 18. The PDFs of particle size in regions I and II resemble the PDF along the entire vertical centerline of the pipe, due to the majority of the particles being located in these two regions. Particles located in region III have a

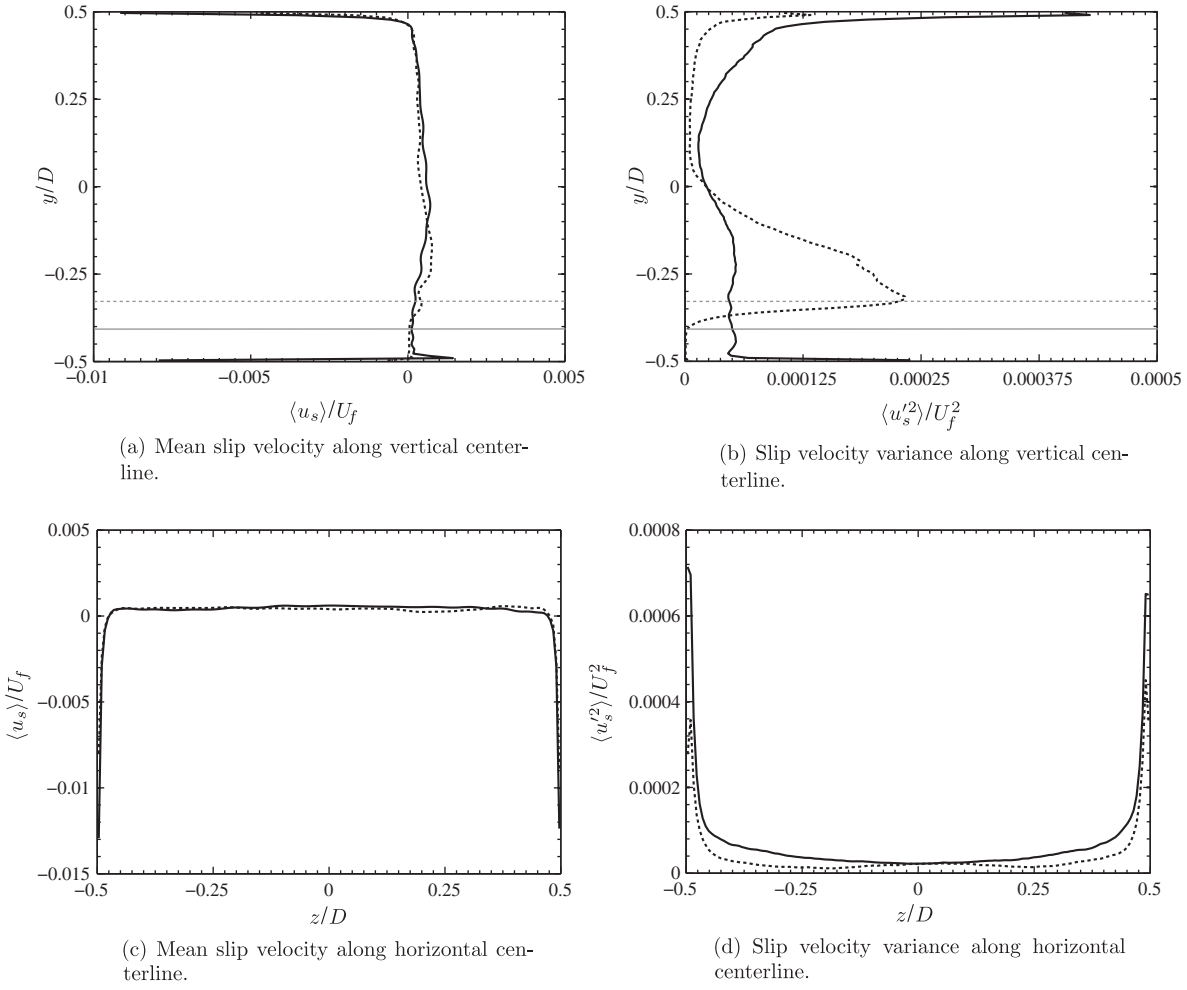

(a) Mean slip velocity along vertical centerline.

(b) Slip velocity variance along vertical centerline.

(c) Mean slip velocity along horizontal centerline.

(d) Slip velocity variance along horizontal centerline.

Fig. 13. Streamwise slip velocity statistics for case A (thick solid line) and case B (dashed line) normalized by the bulk streamwise velocity. The thin gray line separates regions II and III in case A and regions I and II in case B. The gray dotted line separates region II and III in case B.

narrower PDF, with much fewer large particles and more small particles. Clearly, the width of the PDF is seen to correspond to the magnitude of particle size fluctuations, where the lower regions of the pipe contain a greater variety of particle sizes and thus larger fluctuations compared to the upper region.

4. Investigating turbulence closures

In the literature, Reynolds-averaged modeling of the kinetic theory of granular flows (Jenkins and Savage, 1983) is commonly used for the computation of turbulent slurries (e.g., Ling et al., 2003; Ekambara et al., 2009; Kaushal et al., 2012; Azimi et al., 2012). A recent study by Fox (2013) derived a consistent framework for investigating RANS of particle-laden turbulence. In the study, it is pointed out that closure models for the fluid phase equations can be taken from turbulence models used for variable-density turbulence, and closure models developed for compressible turbulence can be used to close the particle-phase terms. However, the coupling terms that involve Reynolds-averaging with respect to both the particle and the fluid properties require further investigation. The simulation results in Section 3.4 can provide useful insight on the relative importance of some of these closures and the validity of existing models.

The covariance of concentration and fluid velocity, referred to as the drift velocity, appears in the Reynolds-averaged fluid-phase transport equations. This term is usually treated as a turbulent flux (Zuber, 1965), and simplifies to

$$\left\langle \varepsilon_p' \boldsymbol{u}_f' \right\rangle = -\frac{\mu_t}{\rho_f \mathrm{Sc}_t} \nabla \langle \varepsilon_p \rangle, \tag{25}$$

where Sc_t is a turbulent Schmidt number that varies with the Stokes number. In a statistically homogeneous flow where the concentration gradient vanishes, this model becomes insufficient, and the following model was proposed for homogeneous directions by Fox (2013):

$$\left\langle \varepsilon_p' \boldsymbol{u}_f' \right\rangle = C_g \langle \varepsilon_p \rangle \langle \varepsilon_f \rangle (\langle \boldsymbol{u}_p \rangle - \langle \boldsymbol{u}_f \rangle), \tag{26}$$

where C_g is a model constant that depends on the particle Reynolds number. Eqs. (25) and (26) are plotted against simulation results in Figs. 19 and 20, respectively, where μ_t was computed from the turbulent-viscosity hypothesis (Pope, 2000)

$$\langle u_f v_f \rangle = -\frac{1}{\rho_f} \mu_t \frac{\partial \langle u_f \rangle}{\partial y}. \tag{27}$$

The vertical component of the drift velocity is shown in Fig. 19. In both cases, $\mathrm{Sc}_t = 1.3$ was determined from the simulations, showing very good agreement between the model and the simulation data. In Fig. 20, the model given in Eq. (26) is plotted against the simulation results for the streamwise component of the drift velocity. Due to periodicity, the first term on the right-hand side of Eq. (26)

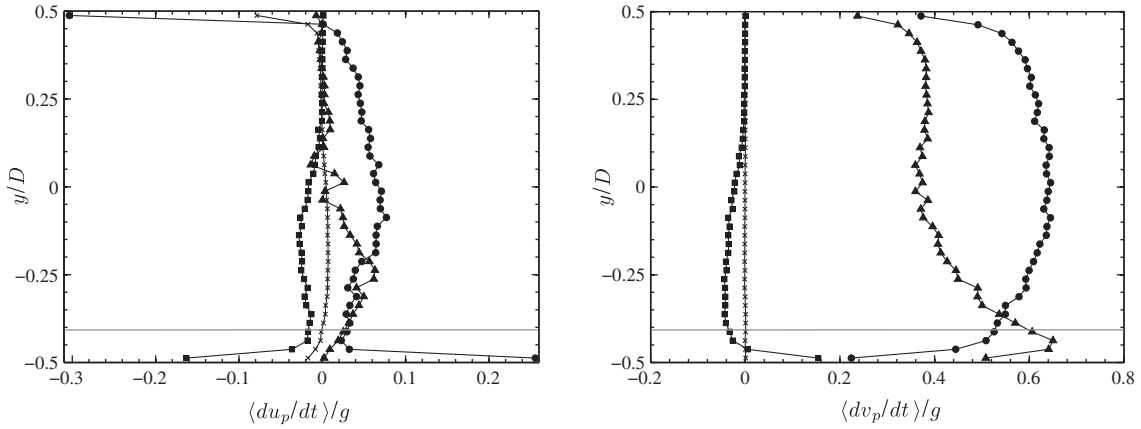

(a) Streamwise particle acceleration for case A.

(b) Vertical particle acceleration for case A.

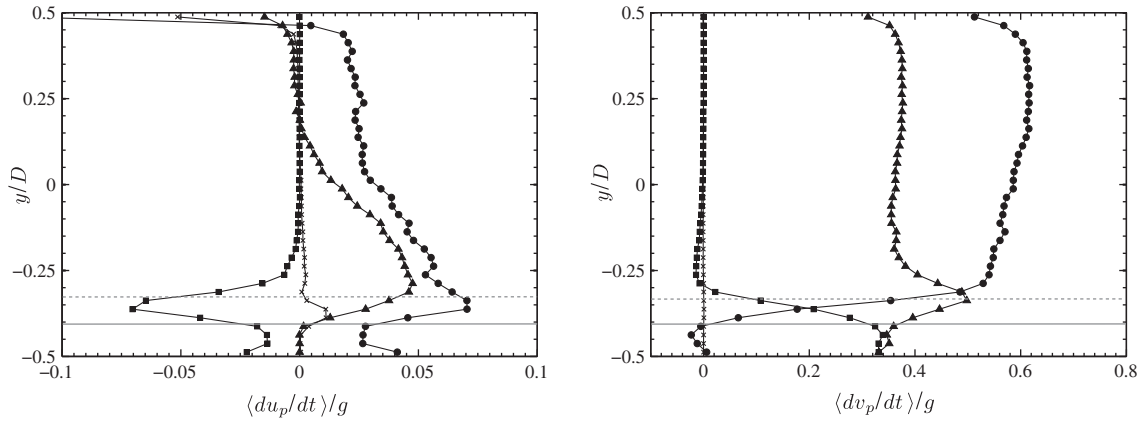

(c) Streamwise particle acceleration for case B.

(d) Vertical particle acceleration for case B.

Fig. 14. Contributing forces to particle acceleration normalized by gravity. Drag as given by Eq. (10) (circles), volume-filtered pressure gradient (triangles), volume-filtered viscous stress (crosses), collisions given by Eqs. (16) and (20) (squares). The thin gray line separates regions II and III in case A and regions I and II in case B. The gray dotted line separates region II and III in case B.

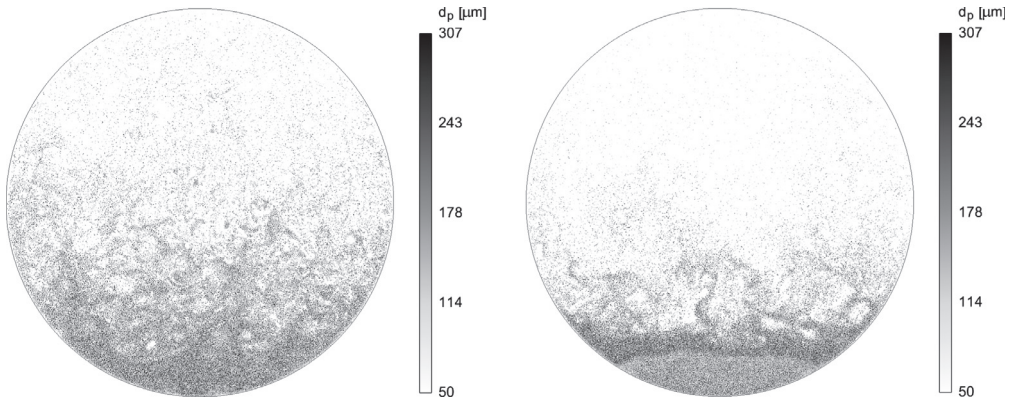

(a) Case A.

(b) Case B.

Fig. 15. Instantaneous snapshot of particle position in an *x*-plane colored by diameter.

vanishes, and $\langle \varepsilon_p' v_f' \rangle$ is shown to be a function of the mean concentration and the difference between the mean velocity of each phase. It was found that an optimal model constant is $C_g = 2.4$ for case A, and $C_g = 1.5$ for case B. With these constants, the model proposed by Fox (2013) is shown to give excellent agreement with the results in this work.

The covariance of volume fraction and fluid pressure gradient appears in the Reynolds-averaged transport equation for the particle velocity (Fox, 2013), and contributes to the mean acceleration of particles due to the fluid. This term represents the fluctuations that contribute to the mean buoyancy force and is often assumed to be negligible. Fig. 21 shows the covariance of volume fraction

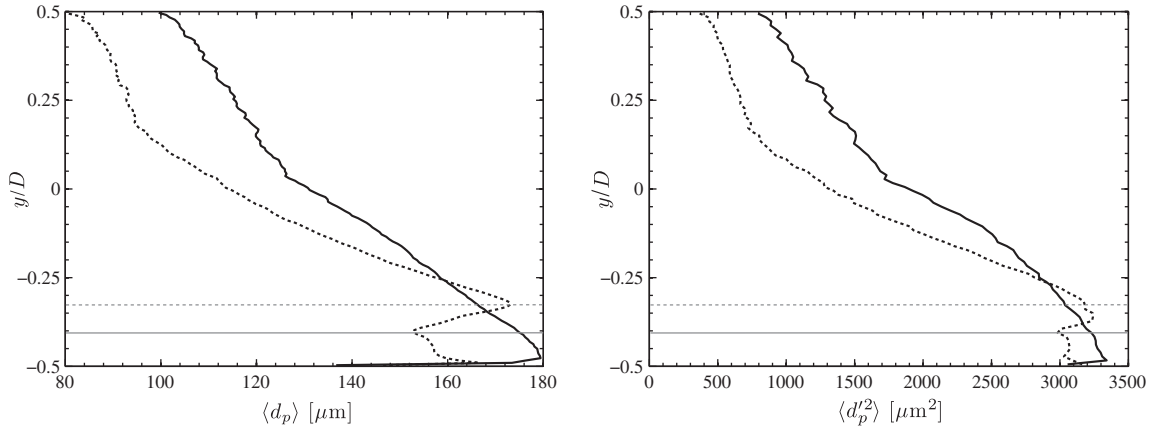

(a) Mean particle size. (b) Particle size variance.

Fig. 16. Particle segregation along pipe centerline for case A (solid line) and case B (dashed line). The thin gray line separates regions II and III in case A and regions I and II in case B. The gray dotted line separates region II and III in case B.

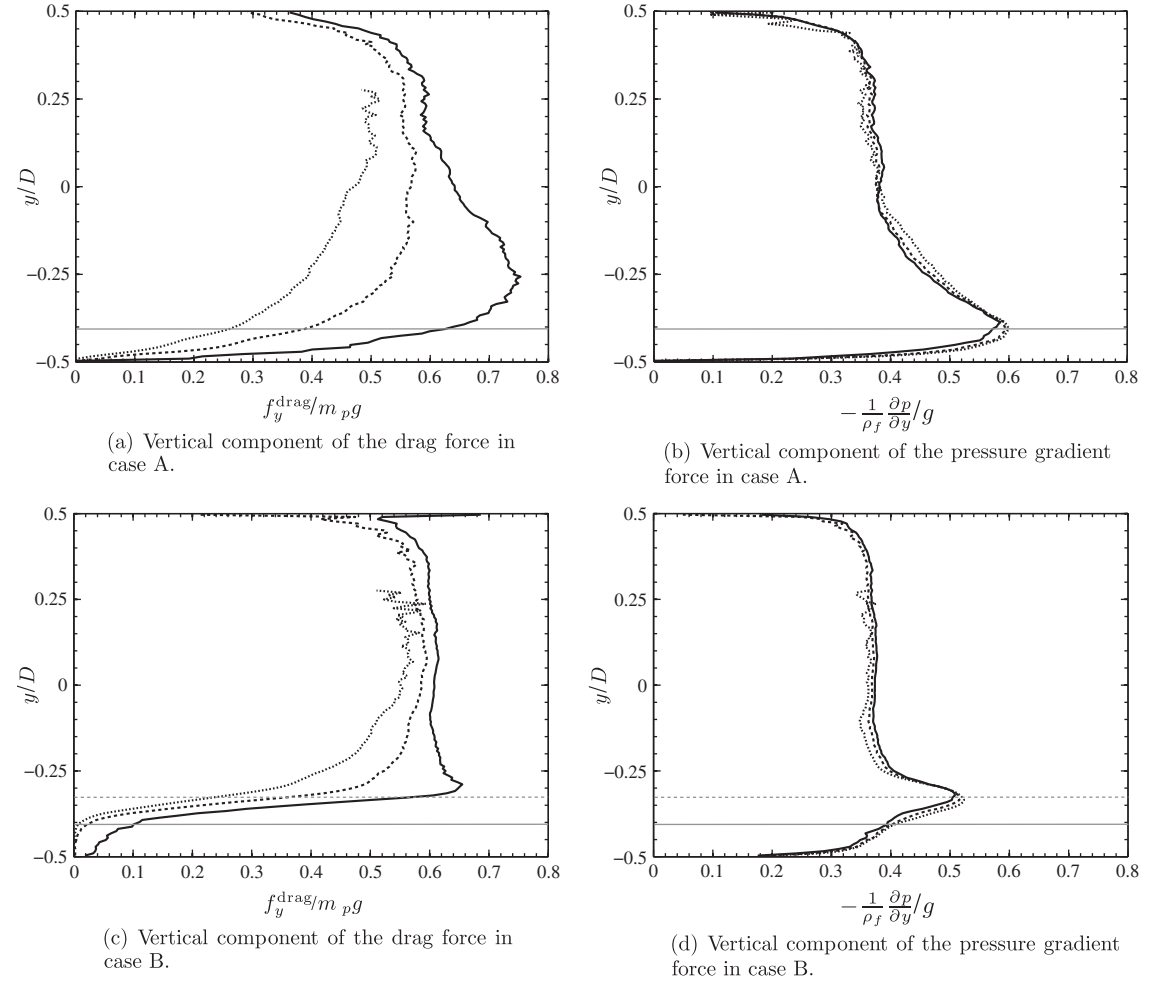

(a) Vertical component of the drag force in case A.

(b) Vertical component of the pressure gradient force in case A.

(c) Vertical component of the drag force in case B.

(d) Vertical component of the pressure gradient force in case B.

Fig. 17. Contributing forces to particle vertical acceleration for different sized particles, normalized by gravity. 50 μm $\leqslant d_p <$ 136 μm (thick solid line), 136 μm $\leqslant d_p <$ 221 μm (dashed line), 221 μm $\leqslant d_p <$ 307 μm (dotted line). The thin gray line separates regions II and III in case A and regions I and II in case B. The gray dotted line separates region II and III in case B.

and fluid pressure gradient normalized by gravity along the vertical axis of the pipe. It is evident that this term contributes little to the particle motion in comparison to the gravitational force, and the assumption to neglect this term in the context of RANS modeling of slurries appears appropriate.

5. Conclusions

A high-fidelity, large eddy simulation framework was coupled with a dense Lagrangian particle tracking solver to investigate horizontal slurry pipe flows operated above and below the critical

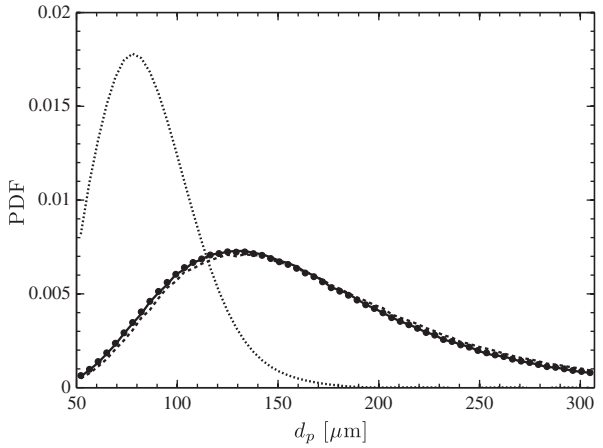

Fig. 18. PDF of particle diameter along the vertical centerline of the pipe in case B. $-0.5 \leqslant y_p/D < -0.405$ corresponding to particles within region I (solid line), $-0.405 \leqslant y_p/D < -0.328$ corresponding to particles within region II (dashed line), $-0.328 \leqslant y_p/D < 0.5$ corresponding to particles in region III (dotted line), and $-0.5 \leqslant y_p/D < 0.5$ corresponding to all of the particles along the vertical centerline (circles).

deposition velocity. The background fluid mesh size was approximately equal to the maximum particle diameter in order to best capture the range of relevant length scales associated with the flow.

Mean particle concentration and velocity profiles were computed, showing excellent agreement with laboratory data. Statistics were extracted for both cases, providing correlations between particle concentration and the velocities of each phase that had otherwise not been investigated in the context of slurries. Three distinct regions were identified in the flow operated below the critical deposition velocity, corresponding to a rigid bed, a highly-collisional shear flow, and a freely-suspended particle flow. The maximum fluctuations in concentration, liquid and particle velocities, and particle diameter were located in the region just above the surface of the bed. In this region, a positive correlation between particle concentration and the vertical velocity of each phase was observed, indicating the tendency for particles to be drawn up from the bed with a greater local concentration than when they fall back to the bed. The statistics presented for the case operated above the critical deposition velocity resemble the lower Reynolds number case shifted by the height of the bed.

Profiles of the particle diameter along the vertical centerline of the pipe reveal a strong segregation in particle size, with the smallest particles located at the top of the pipe and the largest towards the bottom. Interestingly, the slurry operated below the critical deposition velocity showed the largest particles to be located just above the surface of the bed. Profiles of the fluid drag and pressure gradient exerted on each particle indicate that the smallest particles in this region experience greater vertical accelerations, leading to a suspension of the largest particles. Throughout the pipe

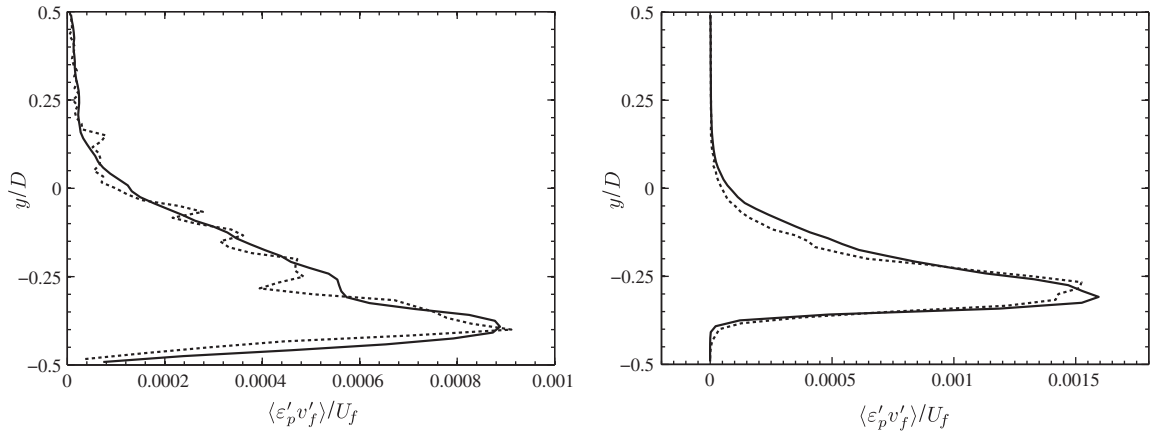

Fig. 19. Vertical component of the drift velocity normalized by the bulk fluid velocity. Simulation results (solid line), model given by Eq. (25) (dashed-line), using $Sc_t = 1.3$.

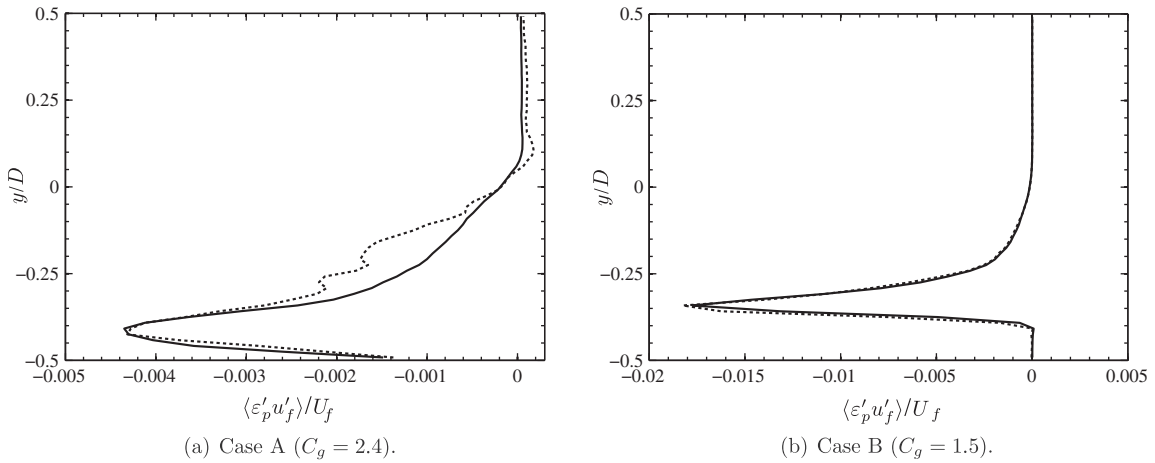

Fig. 20. Streamwise component of the drift velocity normalized by the bulk fluid velocity. Simulation results (solid line), model given by Eq. (26) (dashed-line).

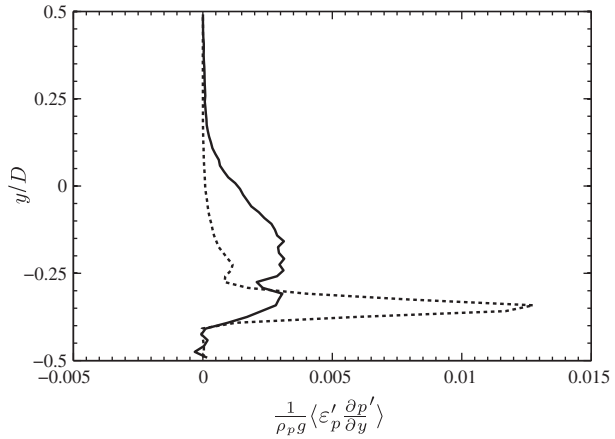

Fig. 21. Normalized covariance of volume fraction and fluid pressure gradient. Case A (solid line), case B (dashed-line).

cross-section, it was observed that the largest contribution to the motion of each particle comes from the drag force, which is opposed by collisions in the streamwise direction and gravity in the vertical direction.

The level of detail provided by the simulations presents a unique opportunity to investigate some of the closures that appear in a recent derivation by Fox (2013) of the exact Reynolds-averaged kinetic theory equations for multiphase flows. The gradient-diffusion model for the vertical drift velocity compared very well with simulation results when setting the turbulent Schmidt number to $Sc_t = 1.3$. The Reynolds number-dependent modeling constant used in a recently proposed model for homogeneous gravity-driven flows (Fox, 2013) was determined for each case, showing excellent agreement with the streamwise drift velocity predicted by the simulations. It was also found that the covariance of fluid pressure gradient and vertical fluid velocity can be neglected in both cases and therefore might often be negligible when modeling turbulent slurries.

Acknowledgement

The authors gratefully acknowledge the financial support of the Shell Oil Company.

References

Anderson, T., Jackson, R., 1967. Fluid mechanical description of fluidized beds: equations of motion. Indus. Eng. Chem. Fundam. 6, 527–539.
Azimi, A.H., Zhu, D.Z., Rajaratnam, N., 2012. Computational investigation of vertical slurry jets in water. Int. J. Multiphase Flow.
Balachandar, S., Eaton, J., 2010. Turbulent dispersed multiphase flow. Annu. Rev. Fluid Mech. 42, 111–133.
Capecelatro, J., Desjardins, O., 2012. An Euler–Lagrange strategy for simulating particle-laden flows. J. Comput. Phys..
Cundall, P., Strack, O., 1979. A discrete numerical model for granular assemblies. Geotechnique 29, 47–65.
Deen, N., Van Sint Annaland, M., Van der Hoef, M., Kuipers, J., 2007. Review of discrete particle modeling of fluidized beds. Chem. Eng. Sci. 62, 28–44.
Desjardins, O., Blanquart, G., Balarac, G., Pitsch, H., 2008. High order conservative finite difference scheme for variable density low Mach number turbulent flows. J. Comput. Phys. 227, 7125–7159.
Doron, P., Granica, D., Barnea, D., 1987. Slurry flow in horizontal pipes experimental and modeling. Int. J. Multiphase Flow 13, 535–547.
Durand, R., Condolios, E., 1952. Hydraulic transportation of coal and solid material in pipes. In: London Colloquium of the National Coal Board.
Ekambara, K., Sanders, R., Nandakumar, K., Masliyah, J., 2009. Hydrodynamic simulation of horizontal slurry pipeline flow using ansys-cfx. Indus. Eng. Chem. Res. 48, 8159–8171.
Fox, R., 2012. Large-eddy-simulation tools for multiphase flows. Annu. Rev. Fluid Mech..
Fox, R., 2013. On multiphase turbulence models for collisional fluid-particle flows. J. Fluid Mech..
Germano, M., Piomelli, U., Moin, P., Cabot, W., 1991. A dynamic subgrid-scale eddy viscosity model. Phys. Fluids A: Fluid Dynam. 3, 1760.
Gibilaro, L., Gallucci, K., Di Felice, R., Pagliai, P., 2007. On the apparent viscosity of a fluidized bed. Chem. Eng. Sci. 62, 294–300.
Gidaspow, D., 1994. Multiphase Flow and Fluidization: Continuum and Kinetic Theory Descriptions. Academic Press.
Gillies, R., Shook, C., Wilson, K., 1991. An improved two layer model for horizontal slurry pipeline flow. Can. J. Chem. Eng. 69, 173–178.
Van der Hoef, M., Ye, M., van Sint Annaland, M., Andrews, A., Sundaresan, S., Kuipers, J., 2006. Multiscale modeling of gas-fluidized beds. Adv. Chem. Eng. 31, 65–149.
Jenkins, J., Savage, S., 1983. A theory for the rapid flow of identical, smooth, nearly elastic, spherical particles. J. Fluid Mech. 130, 187–202.
Kaushal, D., Thinglas, T., Tomita, Y., Kuchii, S., Tsukamoto, H., 2012. CFD modeling for pipeline flow of fine particles at high concentration. Int. J. Multiphase Flow.
Kaushal, D., Tomita, Y., 2002. Solids concentration profiles and pressure drop in pipeline flow of multisized particulate slurries. Int. J. Multiphase Flow 28, 1697–1717.
Kaushal, D., Tomita, Y., 2007. Experimental investigation for near-wall lift of coarser particles in slurry pipeline using γ-ray densitometer. Powder Technol. 172, 177–187.
Kumar, U., Mishra, R., Singh, S., Seshadri, V., 2003. Effect of particle gradation on flow characteristics of ash disposal pipelines. Powder Technol. 132, 39–51.
Kurose, R., Komori, S., 1999. Drag and lift forces on a rotating sphere in a linear shear flow. J. Fluid Mech. 384, 183–206.
Lilly, D., 1992. A proposed modification of the germano subgrid-scale closure method. Phys. Fluids A: Fluid Dynam. 4, 633.
Ling, J., Skudarnov, P., Lin, C., Ebadian, M., 2003. Numerical investigations of liquid–solid slurry flows in a fully developed turbulent flow region. Int. J. Heat Fluid Flow 24, 389–398.
Meneveau, C., Lund, T., Cabot, W., 1996. A Lagrangian dynamic subgrid-scale model of turbulence. J. Fluid Mech. 319, 353–385.
Meyer, M., Devesa, A., Hickel, S., Hu, X., Adams, N., 2010. A conservative immersed interface method for Large-Eddy Simulation of incompressible flows. J. Comput. Phys..
Orszag, S.A., Yakhot, V., Flannery, W.S., Boysan, F., Choudhury, D., Maruzewski, J., Patel, B., 1993. Renormalization group modeling and turbulence simulations. Near-wall Turbul. Flows, 1031–1046.
Patankar, N., Joseph, D., 2001. Modeling and numerical simulation of particulate flows by the Eulerian–Lagrangian approach. Int. J. Multiphase Flow 27, 1659–1684.
Pepiot, P., Desjardins, O., 2010. Direct numerical simulation of dense particle-laden flows using a conservative immersed boundary technique. In: Proceedings of the Summer Program, p. 323.
Pierce, C., 2001. Progress-variable approach for large-eddy simulation of turbulent combustion. Ph.D. thesis, Citeseer.
Pope, S.B., 2000. Turbulent Flows. Cambridge University Press.
Pozorski, J., Apte, S., 2009. Filtered particle tracking in isotropic turbulence and stochastic modeling of subgrid-scale dispersion. Int. J. Multiphase Flow 35, 118–128.
Roco, M., Balakrishnam, N., 1985. Multi-dimensional flow analysis of solid–liquid mixtures. J. Rheol. 29, 431–456.
Saffman, P., 1965. The lift on a small sphere in a slow shear flow. J. Fluid Mech. 22, 385–400.
Schaan, J., Sumner, R., Gillies, R., Shook, C., 2000. The effect of particle shape on pipeline friction for newtonian slurries of fine particles. Can. J. Chem. Eng. 78, 717–725.
Tenneti, S., Garg, R., Subramaniam, S., 2011. Drag law for monodisperse gas–solid systems using particle-resolved direct numerical simulation of flow past fixed assemblies of spheres. Int. J. Multiphase Flow 37, 1072–1092.
Wang, Q., Squires, K., Chen, M., McLaughlin, J., 1997. On the role of the lift force in turbulence simulations of particle deposition. Int. J. Multiphase Flow 23, 749–763.
Wasp, E., Kenny, J., Gandhi, R., 1977. Solid–liquid flow: slurry pipeline transportation [pumps, valves, mechanical equipment, economics]. Ser. Bulk Mater. Handl.(United States) 1.
Wilson, K., 1976. A unified physically-based analysis of solid–liquid pipeline flow. In: Proceedings Hydrotransport, pp. 1–16.
Zhang, D., Prosperetti, A., 1994. Averaged equations for inviscid disperse two-phase flow. J. Fluid Mech. 267, 185–220.
Zuber, N., 1965. Average volumetric concentration in two-phase flow systems. J. Heat Transfer 87, 453–464.